



**HAL**  
open science

## **Simulation Studies of Methane, Carbon Dioxide, Hydrogen, and Deuterium in ITQ-1 and NaX Zeolites**

George K Papadopoulos, Doros N Theodorou

► **To cite this version:**

George K Papadopoulos, Doros N Theodorou. Simulation Studies of Methane, Carbon Dioxide, Hydrogen, and Deuterium in ITQ-1 and NaX Zeolites. *Molecular Simulation*, 2009, 35 (01-02), pp.79-89. <10.1080/08927020802468380>. <hal-00515060>

**HAL Id: hal-00515060**

**<https://hal.science/hal-00515060v1>**

Submitted on 4 Sep 2010

**HAL** is a multi-disciplinary open access archive for the deposit and dissemination of scientific research documents, whether they are published or not. The documents may come from teaching and research institutions in France or abroad, or from public or private research centers.

L'archive ouverte pluridisciplinaire **HAL**, est destinée au dépôt et à la diffusion de documents scientifiques de niveau recherche, publiés ou non, émanant des établissements d'enseignement et de recherche français ou étrangers, des laboratoires publics ou privés.



HAL Authorization

## Simulation Studies of Methane, Carbon Dioxide, Hydrogen, and Deuterium in ITQ-1 and NaX Zeolites

Journal:	<i>Molecular Simulation/Journal of Experimental Nanoscience</i>
Manuscript ID:	GMOS-2008-0156.R1
Journal:	Molecular Simulation
Date Submitted by the Author:	06-Sep-2008
Complete List of Authors:	Papadopoulos, George; National Technical University of Athens, Chemical Engineering Theodorou, Doros; National Technical University of Athens, Chemical Engineering
Keywords:	Molecular dynamics, NaX, ITQ-1, Hydrogen, Carbon dioxide

SCHOLARONE™  
Manuscripts

1  
2  
3 **SIMULATION STUDIES OF METHANE, CARBON DIOXIDE,**  
4  
5 **HYDROGEN, AND DEUTERIUM IN ITQ-1 AND NaX ZEOLITES**  
6  
7  
8  
9  
10  
11  
12  
13  
14  
15  
16  
17  
18  
19  
20  
21

22 George K. Papadopoulos and Doros N. Theodorou  
23  
24

25  
26  
27 *School of Chemical Engineering, National Technical University of Athens, 9 Heroon*  
28  
29 *Polytechniou Street, 157 80 Athens, Greece.*  
30  
31  
32  
33  
34  
35  
36  
37  
38  
39  
40  
41  
42  
43  
44  
45  
46  
47  
48  
49  
50  
51  
52  
53  
54  
55  
56  
57

58 **gkpap@chemeng.ntua.gr (George K. Papadopoulos)**  
59

60 **doros@central.ntua.gr (Doros N. Theodorou)**

**Abstract**

The sorption dynamics of methane, carbon dioxide, hydrogen and deuterium in digitally reconstructed frameworks of ITQ-1 and NaX zeolites was investigated via atomistic and mesoscopic computer simulations. The loading dependence of the self-diffusivity proved to be affected by the energetic inhomogeneity of the sorption sites or/and their topology in the particular crystal. Collective (Maxwell – Stefan) and hence transport diffusivities are examined on the basis of sorbate–sorbate interactions via a jump diffusion model invoking Quasichemical mean field theory.

## 1. Introduction

The efficient design of nanoporous sorbents for reaction, separation, or environmental engineering processes requires a systematic study of the dynamical properties of sorbate molecules confined in the interior of these materials, which may be either crystalline, or amorphous. This type of study typically deals with a multicomponent sorbed phase inside a porous crystalline (e.g. zeolites) or amorphous (e.g. carbon molecular sieves, carbon nanotubes) sorbent material; under the conditions used in the majority of the applications, the solid phase can be considered static without seriously affecting the microscopic flow dynamics of the system [1].

Apart from the strong technology-oriented incentives for studying the dynamics of fluids in pore systems, revealing the physical aspects affecting the transport of the sorbed phase is of great fundamental interest. Among many classes of solids which serve as sorbent materials, structures exhibiting a high degree of order in their atomic-level structure, such as zeolites and more recently zeolitic shape-persistent analogues such as Zeolite Imidazolate, Metal- or Covalent-Organic Frameworks and Titanosilicates, have proved particularly promising. The significant advantage of these materials lies in their well-defined structural characteristics, namely the channel size and shape, the micropore connectivity and the charge distribution due, e.g., to the presence of more than one kinds of tetrahedral (T) atoms in their framework.

Following the macroscopic phenomenological approach, mass transport is studied in terms of flux vectors generated by density or chemical potential gradients in the sorbed phase by invoking either Fick's laws, or Maxwell-Stefan theory and the Onsager formulation, respectively [1 – 3]. The microscopic modelling of diffusion,

1  
2  
3 on the other hand, involves mostly deterministic Molecular Dynamics simulations in  
4 equilibrium (MD) or non-equilibrium (NEMD) ensembles. Atomistic MD cannot  
5 address time scales longer than microseconds with currently available computational  
6 means. In order to overcome this problem, in cases where transport occurs as a  
7 sequence of infrequent jumps between sites in the nanoporous medium, an alternative  
8 way is to identify the sites where penetrant molecules spend most of their time,  
9 compute intersite transition rates atomistically based on infrequent event theory, and  
10 sample stochastic trajectories consisting of long sequences of jumps by Kinetic Monte  
11 Carlo (KMC) simulation. KMC can clearly cover longer time scales; its use  
12 presupposes a time scale separation between the time required for a molecule to  
13 equilibrate within a state, and the waiting time before a jump to another state occurs.  
14 Ref [1] and references therein describe in detail the methodology and the applicability  
15 of dynamically corrected transition-state theory (TST) in conjunction with KMC to  
16 diffusion studies of molecules sorbed in zeolites.

17  
18  
19  
20  
21  
22  
23  
24  
25  
26  
27  
28  
29  
30  
31  
32  
33  
34  
35  
36  
37  
38  
39 In this article we describe an attempt to relate the sorption and diffusion properties of  
40 fluids such as hydrogen, methane, carbon dioxide and their mixtures in pure siliceous  
41 and in anionic aluminosilicate zeolite frameworks containing interstitial and  
42 exchangeable cations. We apply MD and proceed by utilizing the relationship of  
43 transport coefficients and time correlation functions under the equilibrium *NVE*  
44 ensemble, employing the Onsager regression hypothesis as it was later reformulated  
45 in the context of Linear Response Theory [4]. The treatment of transport phenomena  
46 via atomistic simulation has the advantage, in comparison with macroscopic  
47 phenomenology, of predicting diffusivity magnitudes as well as their temperature,  
48 loading and composition dependencies. Also, the predicted results are amenable to  
49  
50  
51  
52  
53  
54  
55  
56  
57  
58  
59  
60

1  
2  
3 comparison with mesoscopic and microscopic experimental measurements, such as  
4 pulsed-field gradient NMR and quasi elastic neutron scattering, respectively, which  
5  
6  
7  
8 have been carried out on a variety of zeolite-guest systems [5 – 9].  
9

## 10 11 12 13 14 15 **2. Computer modelling** 16

### 17 18 19 20 **2.1 Zeolite digitization** 21

22  
23  
24 The procedure we followed for reconstructing a digital crystal entails adopting the  
25 unit cell geometric characteristics that correspond to the particular framework type  
26 code; locating the position vectors of the “primary” framework atoms [10], from the  
27 X-Ray-Diffraction pattern or neutron diffraction data of the crystal; and then applying  
28 the symmetry operations of the space group to which the crystal belongs. The types  
29 and position vectors of all framework and off-framework atoms of the unit cell, taking  
30 into account their occupancy probability found from the XRD analysis or neutron  
31 diffraction data, are finally generated to form a computer model of the unit cell.  
32  
33  
34  
35  
36  
37  
38  
39  
40  
41  
42

43  
44  
45 We constructed a model for the ITQ-1 zeolite framework by employing a double unit  
46 cell instead of the original hexagonal one, for convenience with periodic boundary  
47 conditions. This new unit cell has an orthorhombic shape with axes  
48  $a = 2 \sin(60^\circ) a'$ ;  $b = a'$ ;  $c = c'$  where  $a'$  and  $c'$  are the original hexagonal unit cell  
49 axes. This procedure gave rise to a base-centered orthorhombic unit cell comprising  
50  
51  
52  
53  
54  
55  
56  
57  
58  
59  
60 144 silicon and 288 oxygen atoms, with lattice points located at the centers of large  
cavities of the zeolite [11].

1  
2  
3  
4  
5  
6 The Si/Al ratio in the framework of the charged NaX ( $\text{Na}_{86}\text{Al}_{86}\text{Si}_{106}\text{O}_{384}$ ) FAU crystal  
7  
8 not only determines the anionic charge per unit cell and thereby the number of  
9  
10 cations, but also affects the distribution of cations among the various kinds of sites  
11  
12 present in the unit cell. Because the Al and Si atoms are indistinguishable by the  
13  
14 XRD technique, in several positions the occupation probability for either type of T  
15  
16 atom is less than unity. The notation for the topology of these sites and their  
17  
18 occupancy by sodium cations have been reported in Ref. [10]. In this study we used  
19  
20 the model of Jaramillo and Auerbach [12], which explicitly distinguishes the Si and  
21  
22 Al atoms, attributing different partial charges to the oxygen framework atoms  
23  
24 according to their neighboring bonded T atoms. With this objective, we randomly  
25  
26 distributed Al atoms among the T sites of the framework up to the desired Si/Al ratio,  
27  
28 in such a way that Löwenstein's rule was fulfilled. In addition, the energy of the  
29  
30 crystal was minimized by means of a Simulated Annealing technique (Fig. 1).  
31  
32  
33  
34  
35  
36  
37  
38  
39  
40  
41  
42  
43  
44  
45  
46  
47  
48  
49  
50  
51  
52  
53  
54  
55  
56  
57  
58  
59  
60

< Fig. 1 >

The representation of the bed of NaX crystals discussed in section 3 was obtained using a mesoscopic particle-based reconstruction method, where a prescribed porosity and particle size are provided experimentally. The NaX final configuration was arrived at through a successive series of energy minimizations by means of Molecular Mechanics at constant particle number density. In this work, the zeolite bed consists of octahedral NaX crystals, based on the experimentally measured bed density of  $590 \text{ kg m}^{-3}$ , the crystal density of  $1530 \text{ kg m}^{-3}$  and the porosity of 0.6; the mean crystal

size (edge length of the platonic octahedra) was equal to 30  $\mu\text{m}$  [8].

## 2.2 Guest – host interactions

The triatomic linear molecule of carbon dioxide was modelled as two consecutive dumbbells sharing the central C atom, arranged on a straight line; partial charges were distributed around each molecule so as to reproduce experimental quadrupole moments [13]. The octapole moment of the methane molecule was ignored; thus, methane was represented as one neutral Lennard-Jones sphere with the parameters:  $\varepsilon_{\text{CH}_4\text{-CH}_4}/k_{\text{B}} = 102.5 \text{ K}$ ,  $\sigma_{\text{CH}_4\text{-CH}_4} = 0.362 \text{ nm}$ ;  $\varepsilon_{\text{CH}_4\text{-O}}/k_{\text{B}} = 131.2 \text{ K}$ ,  $\sigma_{\text{CH}_4\text{-O}} = 0.346 \text{ nm}$ ;  $\varepsilon_{\text{CH}_4\text{-Na}}/k_{\text{B}} = 328.3 \text{ K}$ ,  $\sigma_{\text{CH}_4\text{-Na}} = 0.294 \text{ nm}$ . The above values resulted from performing a calibration with respect to measured sorption isotherms; they are able to reproduce satisfactorily a set of experimental data in a temperature range from 120 to 550 K found in Ref. [14]. Hydrogen was also modelled as a single Lennard-Jones site; its strength and size parameters resulted from calibration with respect to bulk experimental data, as explained in Refs 7 and 9 and the references therein.

For the short-ranged sorbate-sorbate and sorbate-zeolite atom interactions the Lennard-Jones potential was used, whereas for hydrogen, the approximation due to Feynman and Hibbs [15] was employed for all dispersion type interactions involved, in order to account for its quantum nature, i.e.,

$$U_{\text{q}}(r_{ij}) = U_{\text{LJ}}(r_{ij}) + \frac{\hbar^2}{24m_{\text{r}}k_{\text{B}}T} \left[ \frac{\partial^2 U_{\text{LJ}}(r_{ij})}{\partial r_{ij}^2} + \frac{2}{r_{ij}} \frac{\partial U_{\text{LJ}}(r_{ij})}{\partial r_{ij}} \right], \quad (1)$$

1  
2  
3  
4  
5  
6 where  $U_{LJ}(r)$  is the Lennard-Jones potential function and  $m_r$  is the reduced mass of the  
7  
8 interacting pair of atoms, given by  $m_r^{-1} = M_i^{-1} + M_j^{-1}$ ;  $M$  denotes molecular mass and  
9  
10 subscripts specify the pair interaction type, e.g. H<sub>2</sub> - H<sub>2</sub> ( $i = j$ ), or H<sub>2</sub> with any atom in  
11  
12 the zeolite framework ( $i \neq j$ ).  
13  
14

15  
16  
17  
18 The long-ranged electrostatic interactions were handled by means of the Ewald  
19  
20 summation technique; the parameters used for the real and reciprocal part of the sums,  
21  
22 as well as the values of partial charges on the sorbate molecules and framework atoms  
23  
24 have been reported in detail elsewhere [10]. In order to reduce the computational  
25  
26 effort associated with both the short- and long-ranged sorbate-sorbent interactions,  
27  
28 when the sorbent was modelled as a rigid framework of atoms, as in the case of the  
29  
30 zeolite crystals studied in this work, we pretabulated these interactions prior to the  
31  
32 actual simulation run on a fine grid running through the pore space of the sorbent.  
33  
34 Sorbate-sorbate interactions, on the other hand, were computed explicitly at each step.  
35  
36  
37  
38  
39  
40

41  
42 Sorption equilibria were studied by means of Grand Canonical Monte Carlo (GCMC)  
43  
44 simulations. These simulations also provided the starting configurations for our MD  
45  
46 simulations of transport. In the case of the faujasite NaX, we need to avoid stochastic  
47  
48 formation of the CO<sub>2</sub> and H<sub>2</sub> molecules inside sodalite cages during GCMC. Sodalite  
49  
50 cages are voluminous enough to accommodate one of these sorbate molecules; yet,  
51  
52 they are inaccessible to these molecules in reality, since the apertures connecting them  
53  
54 to the main pore space are too small to be traversed by the sorbates at any reasonable  
55  
56 rate. After the pretabulation of the entire potential, the interior of sodalite cages was  
57  
58 excluded from the sampling procedure during the Monte Carlo runs; thus, the  
59  
60

1  
2  
3 sampling of intracrystalline space was confined to the physically acceptable regions,  
4  
5 which are determined by the sizes of the CO<sub>2</sub> and H<sub>2</sub> molecules on the one hand and  
6  
7 openings of the sodalite framework on the other. Figure 2 shows our computation of  
8  
9 the electrostatic field within a certain plane in the NaX unit cell.  
10  
11

12  
13  
14  
15 <Fig. 2>  
16  
17

18  
19 The density,  $\rho$ , of sorbate molecules in the zeolite unit cells was computed by means  
20  
21 of GCMC sampling in the form of phase space averages under an imposed set of  
22  
23 chemical potential,  $\mu$ , volume,  $V$ , and temperature,  $T$ , values. In particular, the  
24  
25 version of the GCMC algorithm due to Adams adopted here involves the quantity  $B$ ,  
26  
27 which is related to the excess chemical potential  $\mu^{\text{ex}}$  of the sorbed phase through the  
28  
29 relation:  
30  
31  
32

$$33 \quad B = \frac{1}{k_{\text{B}}T} \mu^{\text{ex}} + \ln \langle N \rangle, \quad (2)$$

34  
35 while  $B$  is related to fugacity,  $f$ , of the bulk phase being in equilibrium with the sorbed  
36  
37 phase according to the equation  
38  
39  
40  
41  
42

$$43 \quad Vf = k_{\text{B}}T \exp(B), \quad (3)$$

44  
45 with  $k_{\text{B}}$  being the Boltzmann constant. In the remainder of this work, fugacity is  
46  
47 approximated by the pressure, assuming that the bulk phase behaves nearly as an ideal  
48  
49 gas.  
50  
51  
52  
53  
54  
55  
56  
57  
58  
59  
60

### 2.3 Transport

The simulations of both methane and xenon were carried out in the standard MD *NVE* ensemble. The MD method creates a set of classical trajectories by integrating the equations of motion for a group of molecules within a fixed volume of zeolite. The equations of motion were formulated in Cartesian coordinates for all sorbate atoms. The sorbate molecules followed classical trajectories, whose time evolution was governed by Newton's equation of motion; the neglect of quantum effects is fully justified at the temperatures of interest here except for H<sub>2</sub>, whose interactions are described by correcting the potentials as described above. The algorithms chosen for the solution of the differential equations of motion for all sorbates studied in this work belong to the category of Störmer-leapfrog integrators.

For the linear molecule of CO<sub>2</sub> the LEN algorithm [13, 16] was applied. It is a leapfrog algorithm in the sense that the quantities saved between time steps are the on-step orientation and the mid-step angular velocity. In particular, in place of angular velocity the rate of change of the bond vector,  $\mathbf{u}$ , is used. Synoptically, if  $\hat{\mathbf{e}}$  is the unit bond vector fixed along the molecule axis, the torque  $\mathbf{T}$  on the molecule can be written as

$$\mathbf{T} = \sum_{\alpha} \mathbf{r}_{\alpha} \times \mathbf{f}_{\alpha} = \hat{\mathbf{e}} \times \sum_{\alpha} d_{\alpha} \mathbf{f}_{\alpha} = \hat{\mathbf{e}} \times \mathbf{g}, \quad (4)$$

with  $\mathbf{g}$  being the “turning force,” which can be determined from the nonbonded forces  $\mathbf{f}_\alpha$  on each atom, the position vectors  $\mathbf{r}_\alpha$  of each interaction site and the (algebraic) distances  $d_\alpha$  of each atom  $\alpha$  from the centre of mass of the linear molecule. In a linear molecule  $\mathbf{g}$  can be replaced by its component perpendicular to the molecular axis,  $\mathbf{g}_p$ , without affecting the torque. The component  $\mathbf{g}_p$  is defined as

$$\mathbf{g}_p = \mathbf{g} - (\hat{\mathbf{e}} \cdot \mathbf{g})\hat{\mathbf{e}}. \quad (5)$$

In order to avoid the use of angular velocity, the time derivative of the axis vector was used:

$$\mathbf{u} = \frac{d\hat{\mathbf{e}}}{dt}. \quad (6)$$

In this algorithm, we applied the constraint that the length of the  $\hat{\mathbf{e}}$  vector remains unity by means of an undetermined Lagrange multiplier [16]. LEN showed remarkable stability, being capable of admitting very large time steps.

The elaboration of molecular dynamics results towards the estimation of transport coefficients, as mentioned in Section 1, relies on linear response theory, which provides the bridge between equilibrium time correlation functions and non-equilibrium response to weak perturbations. The theory also proves that the time integrals of autocorrelation functions are related to transport coefficients via relations known as Green-Kubo. In an averaged form which allows accumulating statistics over all the  $N$  molecules of the system possessing center-of-mass velocities,  $\mathbf{v}_a$ , where

$a = 1, \dots, N$ , and for a three-dimensional system, these relations take the following forms for the self-diffusivity,  $D_s$ , and collective diffusivity,  $D_0$ , respectively:

$$D_s = \frac{1}{3N} \int_0^\infty dt \left\langle \sum_{i=1}^N \mathbf{v}_i(t) \cdot \mathbf{v}_i(0) \right\rangle, \quad (7)$$

$$D_0 = \frac{1}{3N} \int_0^\infty dt \sum_{i=1}^N \sum_{j=1}^N \left\langle \mathbf{v}_i(t) \cdot \mathbf{v}_j(0) \right\rangle. \quad (8)$$

Alternatively, the above equations are usually used in their equivalent well-known Einstein form involving the position vectors of the particles,  $\mathbf{r}_i$ , i.e.,

$$D_s = \frac{1}{6N} \lim_{t \rightarrow \infty} \frac{d}{dt} \left\langle \sum_{i=1}^N [\mathbf{r}_i(0) - \mathbf{r}_i(t)]^2 \right\rangle, \quad (9)$$

$$D_0 = \frac{1}{6N} \lim_{t \rightarrow \infty} \frac{d}{dt} \left\langle \left[ \sum_{i=1}^N [\mathbf{r}_i(0) - \mathbf{r}_i(t)] \right]^2 \right\rangle. \quad (10)$$

A general expression for the isothermal steady-state single component sorbate flow in the absence of external force fields can be written in Fickian form as follows

$$\mathbf{J} = -\mathbf{D}_t(\rho) \cdot \nabla \rho. \quad (11)$$

In the above equation, the vector  $\mathbf{J}$  is the overall macroscopic flux, expressed as the mean number of molecules flowing per unit cross-sectional area in a directional (anisotropic) medium due to a concentration (number density  $\rho$ ) gradient, and  $\mathbf{D}_t$  is

1  
2  
3 the transport diffusivity tensor, which in general can be a function of concentration.  
4  
5 Therefore, in zeolite crystals or textured materials, transport, and consequently self-  
6  
7 and collective diffusivity, have a tensorial character (the reader is reminded that Eqs 7  
8  
9 – 10 are orientational averages); in other words the flux vector depends onto the  
10  
11 spatial orientation of the applied density gradient with respect to the crystal symmetry  
12  
13 axes. In an isotropic medium, Eq. 11 converts to the well known Fick's law defining  
14  
15 the scalar diffusivity.  
16  
17  
18  
19  
20  
21

22 The relation between the (orientationally averaged) transport and collective diffusivity  
23  
24 can be expressed through a Darken-type equation, i.e.,  
25  
26  
27  
28

$$D_1(\rho) = D_0(\rho) \frac{\partial \ln f}{\partial \ln \rho}. \quad (12)$$

29  
30  
31  
32  
33  
34

35 In the preceding lines we have followed the Fickian phenomenological approach to  
36  
37 linking fluxes and concentration gradients. The interested reader can find an  
38  
39 analogous phenomenological development based on chemical potential gradients due  
40  
41 to Onsager, as well as the Stefan – Maxwell formulation, which is based on a balance  
42  
43 of forces exerted on the diffusing particles, in Refs [17, 18] and references therein.  
44  
45  
46  
47  
48  
49  
50  
51  
52  
53  
54  
55  
56

### 57 3. Results and discussion

58  
59  
60

In this section we present results on sorption and diffusion computer experiments on selected siliceous and charged zeolite frameworks. Comparisons with experimental measurements are made, whenever possible.

**<Fig. 3>**

The sorbed phase concentration (loading) inside the crystal was computed by means of Grand Canonical Ensemble Monte Carlo. In Figure 3 the sorption isotherms of methane and carbon dioxide in ITQ-1 are shown for various sets of parameters used to describe the energetics of these systems in previous studies (see caption).

**<Fig. 4>**

The singlet density distribution  $\rho^1(\mathbf{r}_1)$  for finding a molecule of methane at a certain position  $\mathbf{r}_1$ , averaged over all occupancies and all configurations,  $\mathbf{r} = \{\mathbf{r}_1, \mathbf{r}_2, \dots, \mathbf{r}_N\}$ , inside the unit cell, given by the relation

$$\rho^1(\mathbf{r}_1) = \frac{1}{\Xi(\mu, V, T)} \sum_{N=1}^{\infty} \frac{\exp[\mu N / k_B T]}{(N-1)!} \int d^3 r_2 \dots d^3 r_N \exp[-U(\mathbf{r}) / k_B T] \quad (13)$$

is depicted in Figure 4; in this figure we selected low-value isodensity surfaces in order to depict the accessible (void) volume, indicating the two independent pore systems (Large Cavity, LC, and Sinusoidal Channel, SC) of this zeolite.

**<Fig. 5>**

1  
2  
3  
4  
5  
6 In Figure 5, the experimentally measured sorption isotherms showing the results of  
7  
8 GCMC simulation for methane in faujasite X zeolite ( $\text{Na}_{86}\text{X}$ ) are presented for two  
9  
10 temperatures; the location of sorbed methane molecules in the interior of supercages  
11  
12 in a snapshot from the simulation is depicted in Figure 6.  
13  
14

15  
16  
17  
18 <Fig. 6>  
19

20  
21  
22 Figure 7 presents the sorption isotherms of hydrogen and deuterium in  $\text{Na}_{86}\text{X}$  at 100  
23  
24 K. All the host-guest and guest-guest dispersive interactions have been described by  
25  
26 means of the Feynman-Hibbs potential mentioned in the previous section; the effect  
27  
28 of the quantum correction tends to reduce the well depth and shift the whole potential  
29  
30 function to the right, increasing the effective size of the sorbed molecules. In  
31  
32 particular, the lighter hydrogen molecule has a bigger effective size with weaker  
33  
34 energy interaction than deuterium. This relative difference is depicted in Figure 7,  
35  
36 where the deuterium is seen to be sorbed slightly more strongly than hydrogen.  
37  
38  
39  
40  
41  
42

43  
44 <Fig. 7>  
45  
46  
47

48  
49 In Figure 8, self-diffusivity measurements of methane obtained from pulsed field  
50  
51 gradient NMR at 223 K [22] and 300 K [23] in faujasite X zeolite ( $\text{Na}_{86}\text{X}$ ) are shown,  
52  
53 along with results of molecular dynamics under the same conditions.  
54  
55  
56  
57

58 <Fig. 8>  
59  
60

1  
2  
3 Predicted and measured values agree reasonably well, indicating a decrease of the  
4 intra-crystalline CH<sub>4</sub> self-diffusivity as the concentration of sorbed phase increases  
5  
6 inside the NaX. The PFG - NMR and MD values appear significantly different at the  
7  
8 higher temperature, whereas the agreement at 223 K is more satisfactory. PFG -  
9  
10 NMR can sample also the inter-crystalline space in addition to the crystal interior,  
11  
12 which is solely sampled by molecular dynamics. The authors of Refs 22 and 23 state  
13  
14 that molecular exchange between the crystallites and the inter-crystalline space during  
15  
16 the observation time was negligible; hence, the measured signal can be solely  
17  
18  
19  
20  
21  
22  
23  
24

25 <Fig. 9>  
26  
27  
28

29 attributed to the intra-crystalline motion. Therefore, the discrepancy at the higher  
30  
31 temperature may not be attributed to the different length scales probed by PFG - NMR  
32  
33 and MD. In previous studies [8, 24] it was shown that no matter what the intra-  
34  
35 crystalline diffusivity is, a major contribution to the measured effective diffusivity  
36  
37 must be expected from the inter-crystalline diffusivity, as well as from the fraction of  
38  
39 molecules in the intercrystalline space around the crystallites; both quantities are  
40  
41 highly temperature dependent.  
42  
43  
44  
45  
46  
47

48 In Figure 9, results from a Kinetic Monte Carlo simulation of inter-crystalline  
49  
50 diffusivity, of ethane in a bed of NaX crystals as a function of the (pressure and  
51  
52 temperature-dependent) mean free path in the gas phase are shown. The whole  
53  
54 procedure of our KMC involves collisions of molecules in the intercrystalline space  
55  
56 only, being treated in a mean field sense without explicitly considering colliding pairs.  
57  
58  
59  
60 The distance  $l$  traveled between successive collisions is picked from an exponential

1  
2  
3 distribution under the prevailing temperature  $T$  and pressure  $p$ , that is to say random  
4 trajectories are generated in the void space of the medium in such a way that in the  
5 bulk gas the lengths  $l$  between successive collisions follow the exponential  
6 distribution expected from the Poisson stochastic sequence of intermolecular  
7 collisions [8], that is to say,  $\langle l \rangle f(l) = \exp(-l/\langle l \rangle)$ ; where  $f(l)dl$  is the conditional  
8 probability of having a collision-free trajectory length between  $l$  and  $l + dl$ , with the  
9 mean value of  $l$  being denoted by  $\langle l \rangle$ . In the bulk gas phase,  $\langle l \rangle$  is the molecular mean  
10 free path  $\lambda = k_B T / p \sigma_{\text{gas}}^2 \pi \sqrt{2}$ , with  $\sigma_{\text{gas}}$  being the collision diameter of gas molecules.  
11  
12 Reflections upon collision with the isotropic crystal surface are assumed to be diffuse;  
13 that is to say, a new direction of motion is generated according to the cosine law that  
14 ensures equal flux of the emitted molecules from the surface through any elementary  
15 area surrounding the collision point, irrespective of direction. In this way it is ensured  
16 that the probability for a molecule to leave the surface per unit time per unit area on  
17 the surface increases as the angle of reflection approaches the normal to the surface.  
18  
19  
20  
21  
22  
23  
24  
25  
26  
27  
28  
29  
30  
31  
32  
33  
34  
35  
36  
37  
38  
39  
40

41 The left-hand side of Figures 9 shows the high-pressure regime ( $\langle l \rangle = \lambda$ ) where the  
42 overall diffusion process is controlled by frequent intermolecular collisions, and the  
43 right-hand side of the same graph shows the behaviour in the low-pressure regime,  
44 where molecular collisions with the surfaces of NaX crystals in the bed dominate the  
45 overall diffusion process and mean free paths are long ( $\langle l \rangle \gg \lambda$ ); obviously in the  
46 latter regime, for  $\lambda$  values higher than  $\langle l \rangle$  intercrystalline diffusivity remains unaltered  
47  
48  
49  
50  
51  
52  
53  
54  
55  
56  
57 in the bed (see plateau in Figure 9).  
58  
59  
60

<Fig. 10>

The results of Figure 10 for deuterium show a different trend from that observed with methane. Here, both quasi-elastic incoherent neutron scattering and molecular dynamics reveal an increase of the self-diffusivity of deuterium at low densities, followed by a plateau up to 8 molecules per supercage of NaX.

<Fig. 11>

<Fig. 12>

This behaviour may be explained on the basis of the different guest – host interactions for deuterium and methane (cf. Figures 11 and 12). These differences are reflected in the partial molar configurational internal energy of the sorbed species (i.e. devoid of the kinetic energy part,  $U_{ig}$ ),  $\bar{U}_s - U_{ig}$ , as obtained from the covariance between number of molecules and potential energy, divided by the variance in the number of molecules in the course of a GCMC simulation, i.e.,

$$\bar{U}_s - U_{ig} = \frac{\langle NU \rangle - \langle N \rangle \langle U \rangle}{\langle N^2 \rangle - \langle N \rangle^2}. \quad (14)$$

In particular, it is seen that the total partial molar configurational internal energy increases abruptly in the case of deuterium and then decreases slightly as loading increases. Although in methane the net host–guest interactions exhibit a steady increase with loading, the total partial molar configurational internal energy of sorbed molecules remains almost constant; this is because the methane–methane part of the

1  
2  
3 partial molar configurational energy decreases much faster with occupancy compared  
4 to the sorbed deuterium-deuterium interactions (cf. insets in Figures 11 and 12). As a  
5 consequence, deuterium perceives a higher energetic heterogeneity within NaX than  
6 does methane. The most attractive host sites (i.e., those presenting the deepest  
7 minima in the host-hydrogen potential energy field) are occupied first, the molecules  
8 residing in them being less mobile; additional molecules at higher occupancy are  
9 more loosely bound. Thus, an increase in deuterium loading is accompanied by an  
10 increase in self-diffusivity (Figure 10). On the other hand, methane, which feels a  
11 practically homogeneous energetic environment, exhibits a decrease of self-diffusivity  
12 with loading because of enhanced intermolecular collisions at high loadings (Figure  
13 8). The above observed difference in host–guest interactions for the two molecules  
14 gives rise to opposite trends in the concentration dependence of self-diffusivities.  
15  
16  
17  
18  
19  
20  
21  
22  
23  
24  
25  
26  
27  
28  
29  
30  
31  
32  
33

34 <Fig. 13>  
35  
36  
37  
38

39 In a simulation study on ITQ-1 we found a shallow maximum with occupancy in the  
40 self-diffusivity of methane. In this zeolite the pore structure is more complicated than  
41 the one of NaX, with two disconnected pore systems. Two-dimensional diffusion can  
42 occur in each pore system with the  $D_{zz}$  element of the diffusivity tensor being zero.  
43 One pore system exhibits large cavities communicating through narrow necks (Figure  
44 4). In this type of structure we found that the concentration dependence of the self-  
45 diffusivity can be strongly affected by the sorbate density distribution along the  
46 narrow interconnections [25]. Figure 13 shows such a sequence of computed  
47 probability densities for  $\text{CO}_2$  and  $\text{CH}_4$  for various total concentrations inside the ITQ-  
48 1 crystal. Methane prefers to reside at the top and bottom of the large cavities. As  
49  
50  
51  
52  
53  
54  
55  
56  
57  
58  
59  
60

1  
2  
3 occupancy increases, it tends to occupy the middle regions of the large cavities more;  
4  
5 this facilitates entry into and passage through the narrow necks emanating from the  
6  
7 middle regions of the large cavities (see Figure 4), leading to the observed shallow  
8  
9 maximum in self-diffusivity [25].  
10  
11

12  
13  
14  
15 <Fig. 14>  
16

17  
18  
19 In Figures 14 the collective (or else the Maxwell – Stefan [17]) diffusivity and the  
20  
21 transport diffusivity of methane and carbon dioxide in ITQ-1 are presented. The  
22  
23 observed behaviour for carbon dioxide is a continuous decrease of collective  
24  
25 diffusivity as the fugacity (pressure of bulk phase) of the sorbed phase increases. On  
26  
27 the other hand, methane exhibits a slight maximum.  
28  
29  
30  
31  
32  
33

34 <Fig. 15>  
35  
36  
37

38  
39 The effect of concentration on the collective diffusivity of hydrogen in NaX is  
40  
41 presented in Figure 15; in this graph, contrary to the trend observed for methane in the  
42  
43 same zeolite, collective diffusivity shows initially an increase up to a slight maximum  
44  
45 just beyond 4 molecules per supercage. In order to interpret this behaviour we have  
46  
47 previously invoked the Reed and Ehrlich theory, [26] according to which the  
48  
49 occupancy dependence of the collective (or corrected, or else Maxwell – Stefan)  
50  
51 diffusivity can be related to the strength of interactions between the sorbate  
52  
53 molecules. In the lattice model considered by Reed and Ehrlich, this strength is  
54  
55 quantified through the nearest neighbor interaction energy parameter,  $w$ , introduced in  
56  
57 conjunction with the Quasichemical mean field theory of sorption; the coordination  
58  
59  
60

1  
2  
3  
4 number,  $z$ , of the lattice and the saturation capacity  $\rho_m$  are additional parameters of  
5  
6 the model [5, 26].  
7  
8  
9

10  
11 **<Fig. 16>**  
12  
13  
14

15 Figure 16 gives an indicative example of the use of Reed - Ehrlich theory for the case  
16 of hydrogen in NaX. The parameters  $w$ ,  $z$ , were estimated by means of fitting to the  
17 simulation data;  $\rho_m$  was computed by GCMC. According to this simple theory, the  
18 presence of a maximum in the collective diffusivity is a consequence of a weak  
19 (considerably less than  $k_B T$ ) dispersion interaction between co-sorbed hydrogen  
20 molecules. In the same graph is shown the predicted collective diffusivity of  
21 deuterium; this is described better by the theoretical Reed and Ehrlich curve. The  
22 differences seen between H<sub>2</sub> and D<sub>2</sub> in Figure 16 correspond to more attractive  
23 sorbate – sorbate interactions between D<sub>2</sub> molecules as compared to H<sub>2</sub> molecules.  
24  
25  
26  
27  
28  
29  
30  
31  
32  
33  
34  
35  
36  
37  
38  
39

40  
41 **<Fig. 17>**  
42  
43

44 Figure 17 shows three other theoretical plots based on the Reed and Ehrlich theory,  
45 constructed for more attractive sorbate-sorbate interactions. These exhibit  
46 completely different loading dependences, which are reminiscent of the behaviours of  
47 methane and carbon dioxide in ITQ-1 (see Figure 14). One should note that the  
48 model of jumps in a lattice considered by Reed and Ehrlich theory is very simplified,  
49 providing only a qualitative explanation of the occupancy dependence of the  
50 collective diffusivity of fluids under confinement.  
51  
52  
53  
54  
55  
56  
57  
58  
59  
60

#### 4. Conclusions

We have performed simulations at atomistic and mesoscopic levels in order to explore the concentration dependence of the sorbed phase dynamics of polar and non-polar fluids in digitally reconstructed purely siliceous as well as counterion-containing aluminosilicate zeolite frameworks.

For the former category we selected a typical representative belonging to Framework Type Code MWW, the ITQ-1. Sorption and diffusion in this zeolite should differ only slightly from those in the protonated version of its aluminum-containing analogue, MCM-22. In the latter class, a representative of the FAU framework type, Na<sub>86</sub>X, was reconstructed. The Si/Al ratio in the frame of this type determines the anionic charge, and therefore the number of cations (counterions) per unit cell. It also affects the distribution of counterions among the various kinds of site present in the unit cell. In the modeling distinct coulombic charges were attributed to all atoms in the framework.

Our molecular dynamics results for the self-diffusivity of methane in NaX show that  $D_s$  decreases as the loading increases; this is in agreement with earlier PFG – NMR intra-crystalline self-diffusivity measurements of other groups [22, 23]. Furthermore, our Kinetic Monte Carlo mesoscopic simulations of inter-crystalline diffusion in an assemblage of NaX crystals predict that the inter-crystalline diffusivity, not captured by atomistic MD simulations, becomes important at high temperatures where Knudsen diffusion becomes dominant.

1  
2  
3  
4  
5  
6 The self-diffusivity of deuterium in NaX, which is predicted in good agreement with  
7  
8 recent QENS measurements, exhibits a monotonic increase with loading. The  
9  
10 energetic heterogeneity experienced by deuterium molecules in NaX proves to be  
11  
12 responsible for this peculiar behaviour, also observed in the case of hydrogen in NaX.  
13  
14 Within ITQ-1, which possesses large elongated cavities with strongly attractive  
15  
16 regions at their top and bottom, connected along their waists by narrow, strongly  
17  
18 attractive pores, the self-diffusivity of methane exhibits a shallow maximum. A  
19  
20 mesoscopic Diffusion through Spatial Discretization approach recently developed in  
21  
22 our group [25] is able to explain this trend.  
23  
24  
25  
26  
27  
28

29 Collective (Maxwell – Stefan) and transport diffusivities of carbon dioxide and  
30  
31 methane in ITQ-1 and also of hydrogen and deuterium in NaX were studied via  
32  
33 atomistic molecular dynamics simulations. Their concentration dependence was  
34  
35 investigated on the basis of the sorbate – sorbate interaction strength invoked by  
36  
37 Quasichemical mean field theory in conjunction with the simple model of Reed and  
38  
39 Ehrlich.  
40  
41  
42  
43  
44  
45

#### 46 **Acknowledgments**

47  
48 We are grateful to Dr E. Pantatosaki and Mr M. Sant for their contribution in the  
49  
50 computational work. Support by the European Union via the FP6-Marie Curie  
51  
52 Research Training Network “INDENS” (MRTN-CT-2004-005503) is gratefully  
53  
54 acknowledged.  
55  
56  
57  
58  
59  
60

## References

- [1] D. N. Theodorou, R. Q. Snurr, A. T. Bell, *Molecular dynamics and diffusion in microporous materials*, in *Comprehensive Supramolecular Chemistry*, Vol. 7, G. Alberti and T. Bein (Eds.), Elsevier, Oxford, 1996, p. 507.
- [2] Auerbach, S. M.F. Jousse, D. P. Vercauteren, *Dynamics of sorbed molecules in zeolites*, in *Computer Modelling of Microporous and Mesoporous Materials*, C. R. A. Catlow, R. A. van Santen, B. Smit (Eds.), Elsevier, Amsterdam, 2004, p. 49.
- [3] G. K. Papadopoulos and D. N. Theodorou, *Computer simulation of sorption and transport in zeolites*, in *Handbook of Heterogeneous Catalysis*, 2<sup>nd</sup> Ed., Vol. 3, G. Ertl, H. Knözinger, F. Schüth and J. Weitkamp (Eds.), p. 1662, Wiley - VCH, Weinheim (2008).
- [4] J. P. Hansen, I. R. McDonald, *Theory of simple liquids*, Academic Press, London, 1986.
- [5] G. K. Papadopoulos, H. Jovic, and D. N. Theodorou, *Transport diffusivity of N<sub>2</sub> and CO<sub>2</sub> in silicalite: Coherent quasielastic neutron scattering measurements and molecular dynamics simulations*, *J. Phys. Chem. B*, **108** (2004), p. 12748.
- [6] G. K. Papadopoulos, *Diffusivity of CH<sub>4</sub> in model silica nanopores: Molecular dynamics and quasichemical mean field theory*, *Mol. Simul.*, **31** (2005), p. 57.

1  
2  
3 [7] A. Kumar, H. Jobic and S. K. Bhatia, *Quantum Effects on Adsorption and*  
4  
5  
6 *Diffusion of Hydrogen and Deuterium in Microporous Materials*, J. Phys. Chem B,  
7  
8 **110** (2006), p. 16666.  
9

10  
11  
12  
13  
14  
15 [8] G. K. Papadopoulos, D. N. Theodorou, S. Vasenkov and J. Kärger, *Mesoscopic*  
16  
17 *simulations of the diffusivity of ethane in beds of NaX zeolite crystals: Comparison*  
18  
19 *with pulsed field gradient NMR measurements*, J. Chem. Phys., **126** (2007), p.  
20  
21 094702.  
22  
23

24  
25  
26  
27  
28  
29 [9] E. Pantatosaki, G. K. Papadopoulos, H. Jobic, and D. N. Theodorou, *A combined*  
30  
31 *atomistic simulation and quasielastic neutron scattering study of the low-temperature*  
32  
33 *dynamics of hydrogen and deuterium confined in NaX zeolite*, J. Phys. Chem. B  
34  
35 (2008), in press.  
36  
37

38  
39  
40  
41 [10] E. Pantatosaki and G. K. Papadopoulos, *On the computation of long-range*  
42  
43 *interactions in fluids under confinement: Application to pore systems with various*  
44  
45 *types of spatial periodicity*, J. Chem. Phys., **127** (2007), p. 164723.  
46  
47  
48

49  
50  
51 [11] J.-M. Leyssale, G. K. Papadopoulos and D. N. Theodorou, *Sorption*  
52  
53 *thermodynamics of CO<sub>2</sub>, CH<sub>4</sub> and their mixtures in the ITQ-1 zeolite as revealed by*  
54  
55 *molecular simulations*, J. Phys. Chem. B, **110** (2006), p. 22742.  
56  
57

58  
59  
60 [12] D. E. Jaramillo and S. M. Auerbach, *New force field for Na cations in faujasite-*

1  
2  
3  
4  
5  
6  
7  
8  
9  
10  
11  
12  
13  
14  
15  
16  
17  
18  
19  
20  
21  
22  
23  
24  
25  
26  
27  
28  
29  
30  
31  
32  
33  
34  
35  
36  
37  
38  
39  
40  
41  
42  
43  
44  
45  
46  
47  
48  
49  
50  
51  
52  
53  
54  
55  
56  
57  
58  
59  
60

*type zeolites*, J. Phys. Chem. B **103** (1999), p. 9589.

[13] K. Makrodimitris, G. K. Papadopoulos and D. N. Theodorou, Prediction of *permeation properties of CO<sub>2</sub> and N<sub>2</sub> through silicalite via molecular simulations*, J. Phys. Chem. B, **105** (2001), p. 777, and references therein.

[14] E. V. Chkhaidze, A. A. Fomkin, V.V. Sepinskii, G. V. Tsitsishvili, *Adsorption of methane on NaX zeolite in the subcritical and supercritical regions*, Bull. Acad. Sci. USSR, Div. Chem. Sci., **34** (1985), p. 886.

[15] R. P. Feynman and A. R. Hibbs,. *Quantum Mechanics and Path Integrals*, McGraw-Hill, New York, 1965

[16] D. Fincham, *Leapfrog Rotational Algorithms for Linear Molecules*, Mol. Simul. **11** (1993), p. 79.

[17] D. Dubbeldam and R. Q. Snurr, *Recent developments in the molecular modeling of diffusion in nanoporous materials*, Mol. Simul., **33** (2007), p. 305.

[18] R. Krishna and J. M. van Baten, *Onsager coefficients for binary mixture diffusion in nanopores*, Chem. Eng. Sci. (2008), in press.

[19] S. J Goodbody,. K.Watanabe, D. MacGovan, J. Walton, and N. Quirke, *Molecular simulation of methane and butane in silicalite*, J. Chem. Soc. Faraday Trans., **87** (1991), p. 1951.

- 1  
2  
3  
4  
5  
6 [20] D. Dubbeldam, S. Calero, T. J. H. Vlugt, R. Krishna, T. Maesen, and B. Smit,  
7  
8 *United atom force field for alkanes in nanoporous materials*, J. Phys. Chem. B, **108**  
9  
10 (2004), p. 12301.  
11  
12  
13  
14  
15 [21] J. G. Harris, K. H. Yung, *Carbon dioxide's liquid-vapor coexistence curve and*  
16  
17 *critical properties as predicted by a simple molecular model*, J. Phys. Chem., **99**  
18  
19 (1995), p. 12021.  
20  
21  
22  
23  
24  
25  
26 [22] J. Kärger, H. Pfeifer, M. Rauscher, and A. Walter, *Self-diffusion of n-paraffins in*  
27  
28 *NaX zeolite*, J. C. S. Faraday I, **76** (1980), p. 717.  
29  
30  
31  
32  
33  
34 [23] J. Caro, M. Bülow, and W. Schirmer, *Microdynamics of methane, ethane and*  
35  
36 *propane in ZSM-5 type zeolites*, J. Chem. Soc., Faraday Trans. I, **81** (1985), p. 2541.  
37  
38  
39  
40  
41 [24] O. Geier, S. Vasenkov, E. Lehmann, J. Kärger, U. Schemmert, R. Rakoczy, J.  
42  
43 *Weitkamp, Interference microscopy investigation of the influence of regular*  
44  
45 *intergrowth effects in MFI-type zeolites on molecular uptake*, J. Phys. Chem. B, **105**  
46  
47 (2001), p. 10217.  
48  
49  
50  
51  
52  
53 [25] M. Sant, G. K. Papadopoulos and D. N. Theodorou, *A second-order Markov*  
54  
55 *process for modeling diffusive motion through spatial discretization*, J. Chem. Phys.  
56  
57 **128** (2008), p. 024504; M. Sant, J.-M. Leyssale, G. K. Papadopoulos, and D.N.  
58  
59 Theodorou, in preparation.  
60

- 1  
2  
3  
4  
5 [26] D. A. Reed and G. Ehrlich, *Surface diffusion, atomic jump rates and*  
6 *thermodynamics*, Surface Sci. **102** (1981), p. 588.  
7  
8  
9  
10  
11  
12  
13  
14  
15  
16  
17  
18  
19  
20  
21  
22  
23  
24  
25  
26  
27  
28  
29  
30  
31  
32  
33  
34  
35  
36  
37  
38  
39  
40  
41  
42  
43  
44  
45  
46  
47  
48  
49  
50  
51  
52  
53  
54  
55  
56  
57  
58  
59  
60

For Peer Review Only

### Captions to figures

**Figure 1.** Indicative total energy plateau during the simulated annealing minimization procedure in NaY [10]; the last runs locating the minimum global energy of the crystal are depicted in the inset.

**Figure 2.** Indicative computed electrostatic field contours for NaX, at  $z = 2.27$  nm. The sodalite interiors, which are removed from the mapping, are evident as open circular regions.

**Figure 3.** Sorption isotherms of CH<sub>4</sub> for two sets of parameters [19, 20] and of the EPM2 model of CO<sub>2</sub> [21] at various temperatures within ITQ-1.

**Figure 4.** Lowest value isodensity surface of CH<sub>4</sub> in ITQ-1 at a total loading of 20.4 (LC) plus 8.6 (SC) molecules per unit cell

**Figure 5.** Measured [14] and predicted sorption isotherms of CH<sub>4</sub> in NaX.

**Figure 6.** Distribution of CH<sub>4</sub> (white spheres) in the Na<sub>86</sub>X framework, depicting the host sorption areas (supercages) at a loading of 9.16 molecules per supercage at 300 K.

**Figure 7.** Simulated sorption isotherms at 100 K for D<sub>2</sub> (red symbols) and H<sub>2</sub> (green symbols) in NaX.

1  
2  
3 **Figure 8.** Comparison of self-diffusivity data obtained via PFG-NMR measurements  
4 at 223 K [22] and 300 K [23], with molecular dynamics simulations for CH<sub>4</sub> in NaX  
5 as a function of loading.  
6  
7  
8  
9

10  
11  
12 **Figure 9.** Intercrystalline self-diffusivity of C<sub>2</sub>H<sub>6</sub> computed via Kinetic Monte Carlo  
13 simulation in a reconstructed bed of octahedral NaX crystals with porosity 0.40 as a  
14 function of mean free path  $\lambda$ .  
15  
16  
17  
18  
19

20  
21  
22 **Figure 10.** Self-diffusivities of D<sub>2</sub> in NaX measured by QENS at 100 K [9] (open  
23 symbols), and results computed by MD under the same conditions (filled symbols) as  
24 a function of sorbate loading.  
25  
26  
27  
28  
29

30  
31  
32 **Figure 11.** Partial molar configurational internal energy, of sorbed H<sub>2</sub> in NaX  
33 calculated from GCMC simulations at a temperature of 100 K and various loadings  
34 (squares); contributions to this quantity from H<sub>2</sub> – NaX interactions (triangles), and  
35 from H<sub>2</sub> – H<sub>2</sub> interactions (inset) are also shown.  
36  
37  
38  
39  
40

41  
42  
43 **Figure 12.** Same as Figure 11 for CH<sub>4</sub> in NaX at 300 K.  
44  
45  
46  
47

48  
49 **Figure 13.**  $xy$  probability densities for CO<sub>2</sub> (a, b, c) and CH<sub>4</sub> (d, e, f) sorbates in the  
50 LC pore system of ITQ-1 at  $T = 250$  K. The pressure is 0.006 atm (a, d), 0.95 atm (b,  
51 e) and 52 atm (c, f).  
52  
53  
54  
55  
56

57  
58 **Figure 14.** Collective and transport diffusivities at 300 K for CH<sub>4</sub> (top) and CO<sub>2</sub>  
59 (bottom) in ITQ-1 as a function of pressure of the bulk phase at equilibrium.  
60

1  
2  
3  
4  
5  
6 **Figure 15.** Collective (triangles) and transport (circles) diffusion coefficients  
7  
8 predicted via MD as a function of H<sub>2</sub> loading in NaX.  
9

10  
11  
12 **Figure 16.** Normalized simulated and experimental collective diffusivities for  
13 hydrogen (circles) and deuterium (triangles) in NaX versus fractional occupancies  $\theta =$   
14  $\rho / \rho_m$ , where  $\rho_m$  is the saturation capacity of NaX for H<sub>2</sub>; lines correspond to  
15 theoretical predictions from the Reed and Ehrlich model [26].  
16  
17  
18  
19  
20  
21  
22  
23  
24

25 **Figure 17.** Normalized collective diffusivities versus fractional occupancies  $\theta$  for  
26 various  $w$  values corresponding to theoretical predictions from the Reed and Ehrlich  
27 model [26].  
28  
29  
30  
31  
32  
33  
34  
35  
36  
37  
38  
39  
40  
41  
42  
43  
44  
45  
46  
47  
48  
49  
50  
51  
52  
53  
54  
55  
56  
57  
58  
59  
60

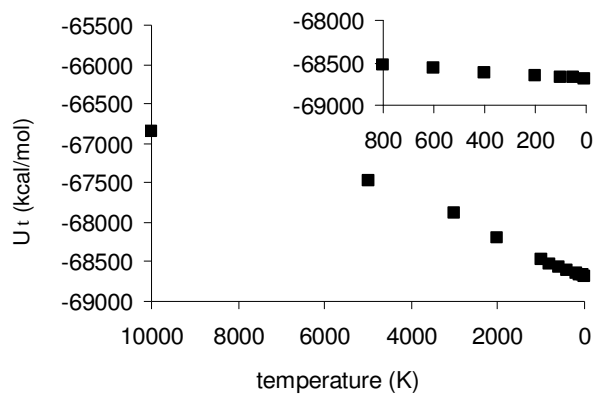


**Fig. 1**

1  
2  
3  
4  
5  
6  
7  
8  
9  
10  
11  
12  
13  
14  
15  
16  
17  
18  
19  
20  
21  
22  
23  
24  
25  
26  
27  
28  
29  
30  
31  
32  
33  
34  
35  
36  
37  
38  
39  
40  
41  
42  
43  
44  
45  
46  
47  
48  
49  
50  
51  
52  
53  
54  
55  
56  
57  
58  
59  
60

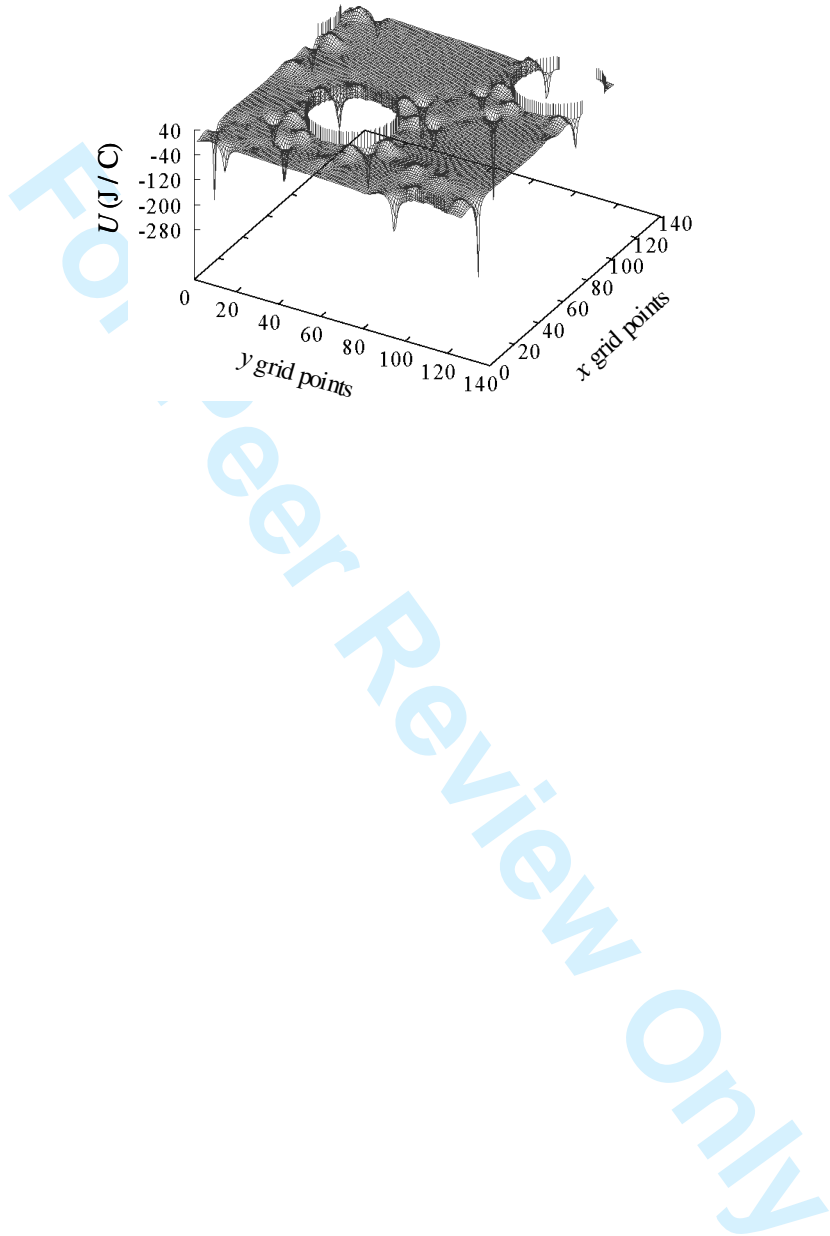


**Fig. 2**

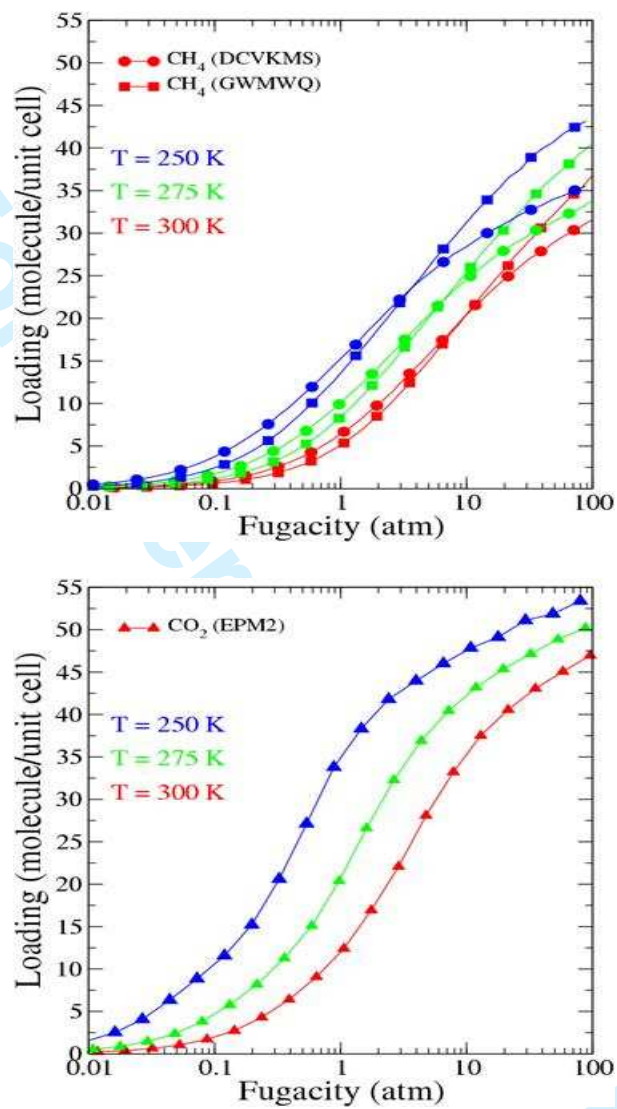
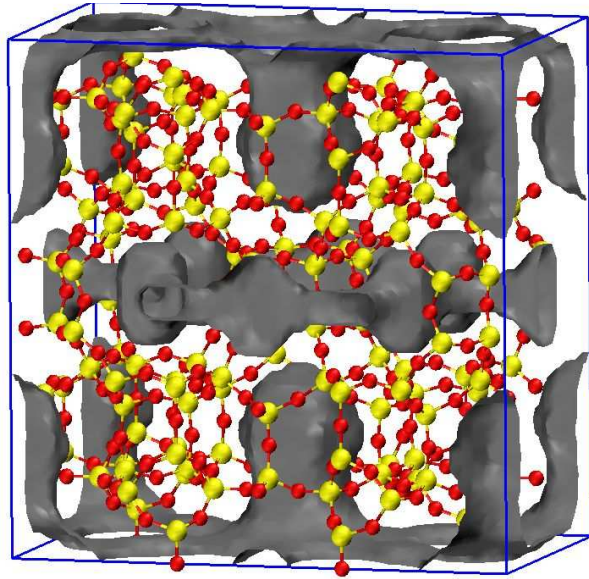


Fig. 3

1  
2  
3  
4  
5  
6  
7  
8  
9  
10  
11  
12  
13  
14  
15  
16  
17  
18  
19  
20  
21  
22  
23  
24  
25  
26  
27  
28  
29  
30  
31  
32  
33  
34  
35  
36  
37  
38  
39  
40  
41  
42  
43  
44  
45  
46  
47  
48  
49  
50  
51  
52  
53  
54  
55  
56  
57  
58  
59  
60



**Fig. 4**

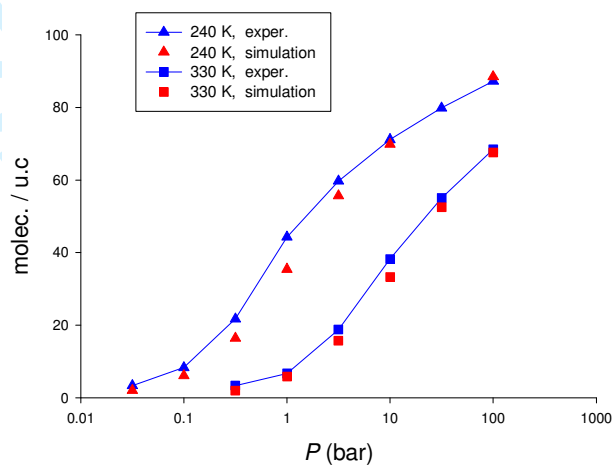
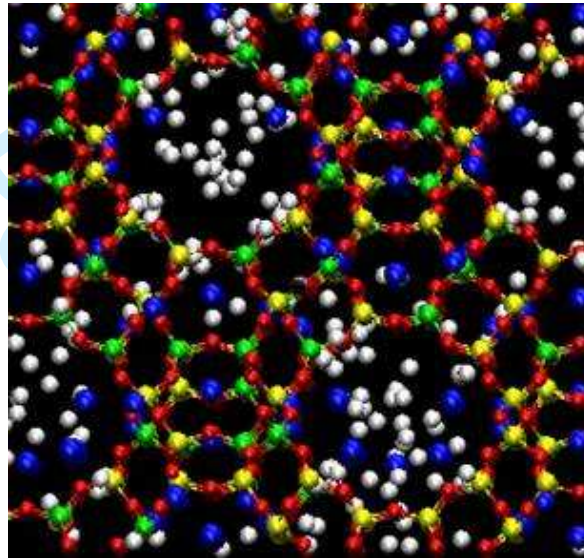


Fig. 5

1  
2  
3  
4  
5  
6  
7  
8  
9  
10  
11  
12  
13  
14  
15  
16  
17  
18  
19  
20  
21  
22  
23  
24  
25  
26  
27  
28  
29  
30  
31  
32  
33  
34  
35  
36  
37  
38  
39  
40  
41  
42  
43  
44  
45  
46  
47  
48  
49  
50  
51  
52  
53  
54  
55  
56  
57  
58  
59  
60



**Fig. 6**

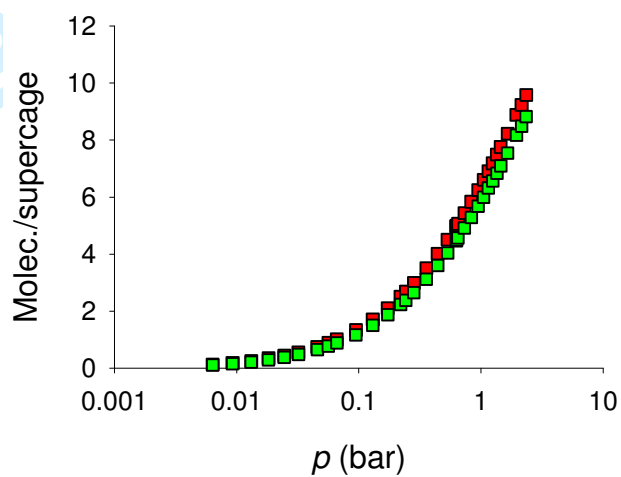


Fig. 7

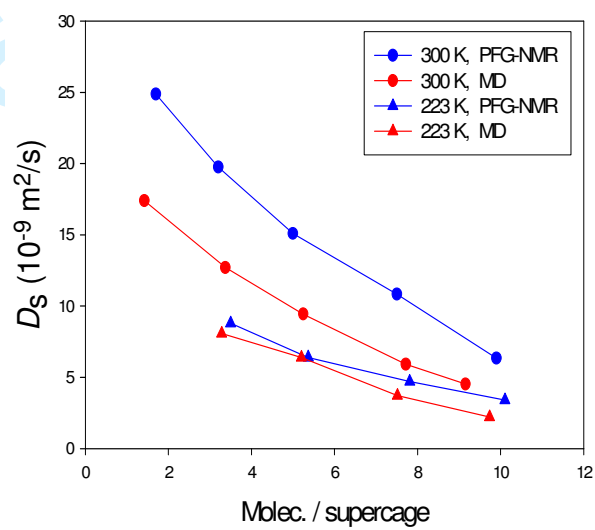
1  
2  
3  
4  
5  
6  
7  
8  
9  
10  
11  
12  
13  
14  
15  
16  
17  
18  
19  
20  
21  
22  
23  
24  
25  
26  
27  
28  
29  
30  
31  
32  
33  
34  
35  
36  
37  
38  
39  
40  
41  
42  
43  
44  
45  
46  
47  
48  
49  
50  
51  
52  
53  
54  
55  
56  
57  
58  
59  
60

Fig. 8

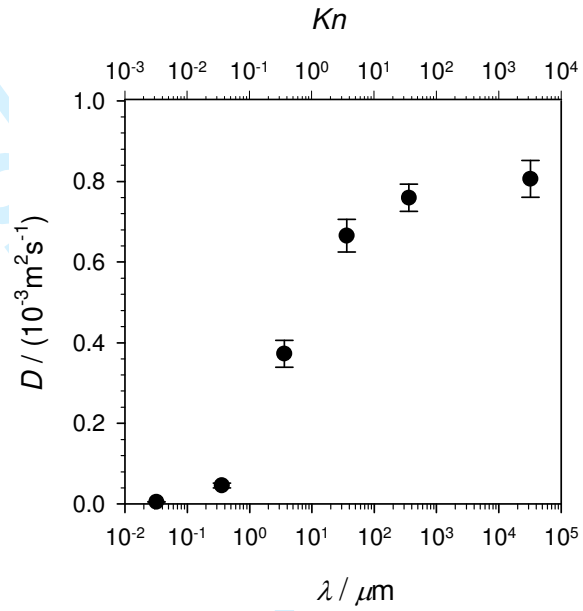


Fig. 9

1  
2  
3  
4  
5  
6  
7  
8  
9  
10  
11  
12  
13  
14  
15  
16  
17  
18  
19  
20  
21  
22  
23  
24  
25  
26  
27  
28  
29  
30  
31  
32  
33  
34  
35  
36  
37  
38  
39  
40  
41  
42  
43  
44  
45  
46  
47  
48  
49  
50  
51  
52  
53  
54  
55  
56  
57  
58  
59  
60

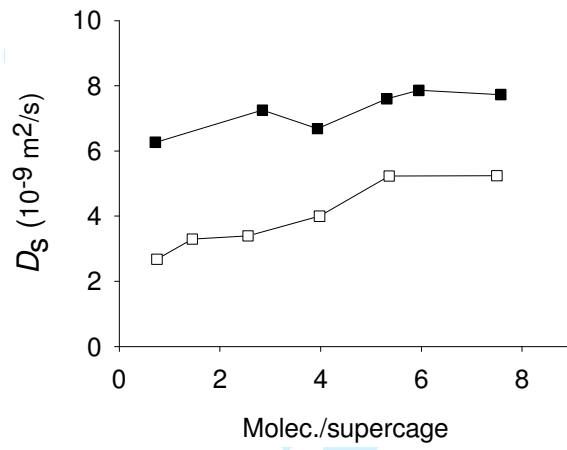


Fig. 10

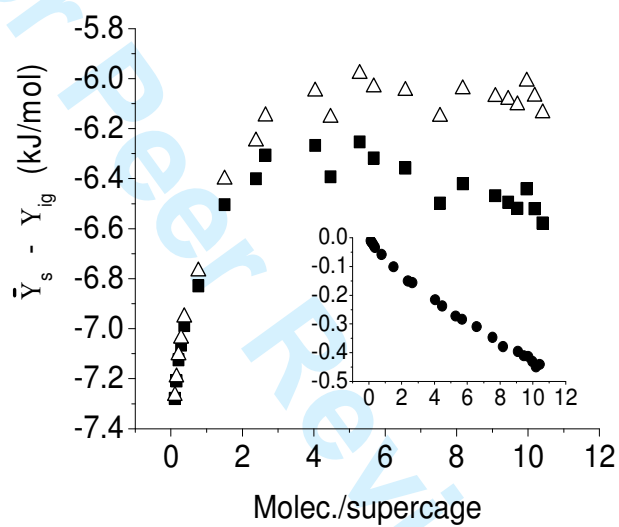


Fig. 11

1  
2  
3  
4  
5  
6  
7  
8  
9  
10  
11  
12  
13  
14  
15  
16  
17  
18  
19  
20  
21  
22  
23  
24  
25  
26  
27  
28  
29  
30  
31  
32  
33  
34  
35  
36  
37  
38  
39  
40  
41  
42  
43  
44  
45  
46  
47  
48  
49  
50  
51  
52  
53  
54  
55  
56  
57  
58  
59  
60

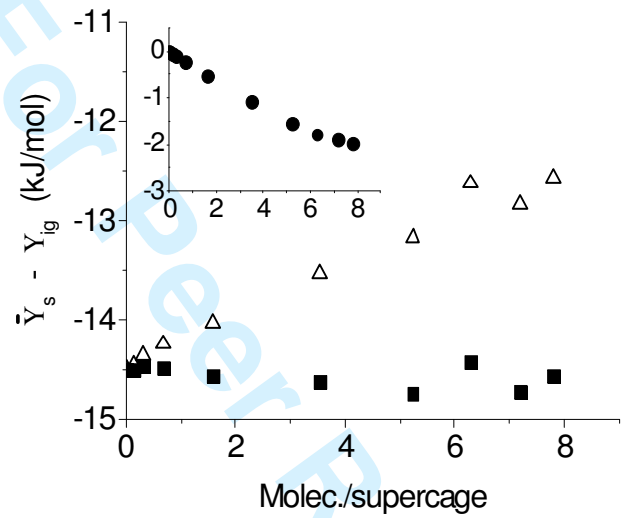


Fig. 12

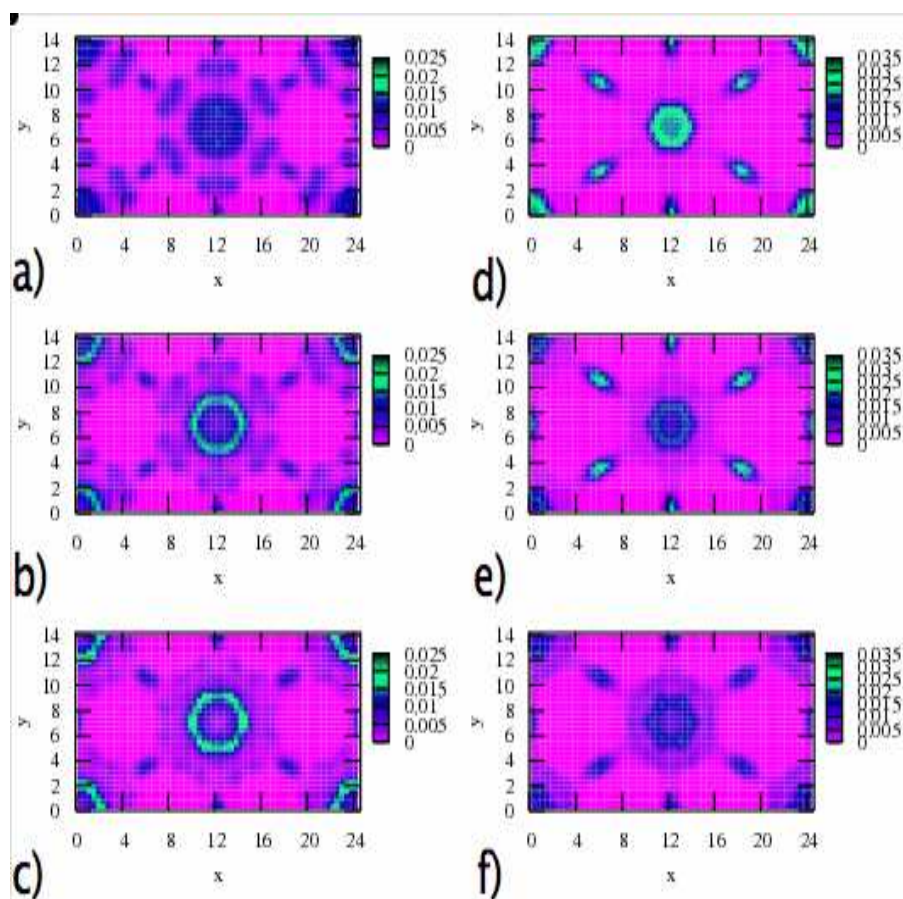


Fig. 13

1  
2  
3  
4  
5  
6  
7  
8  
9  
10  
11  
12  
13  
14  
15  
16  
17  
18  
19  
20  
21  
22  
23  
24  
25  
26  
27  
28  
29  
30  
31  
32  
33  
34  
35  
36  
37  
38  
39  
40  
41  
42  
43  
44  
45  
46  
47  
48  
49  
50  
51  
52  
53  
54  
55  
56  
57  
58  
59  
60

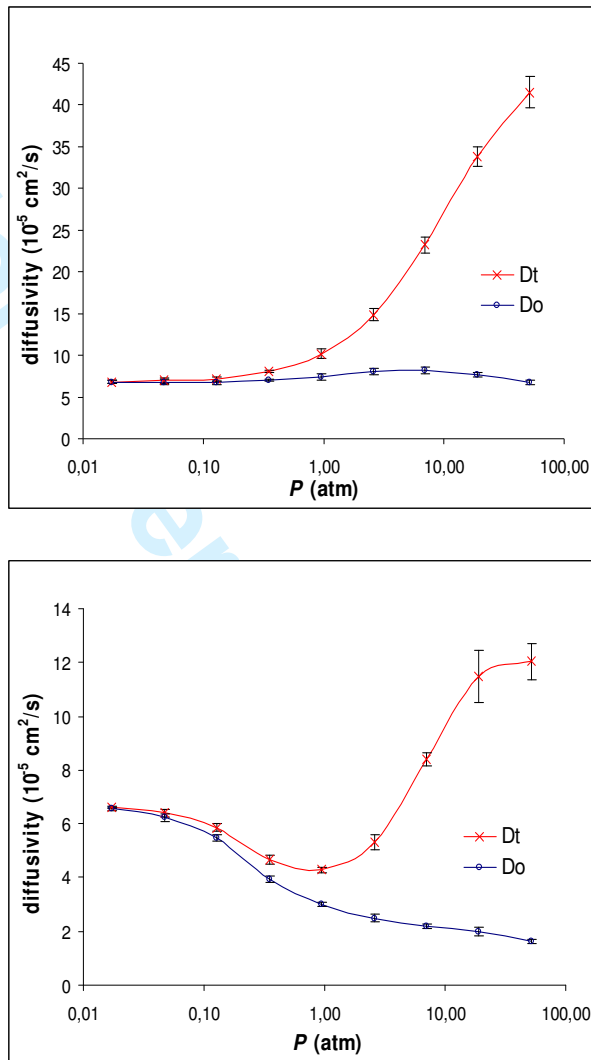


Fig. 14

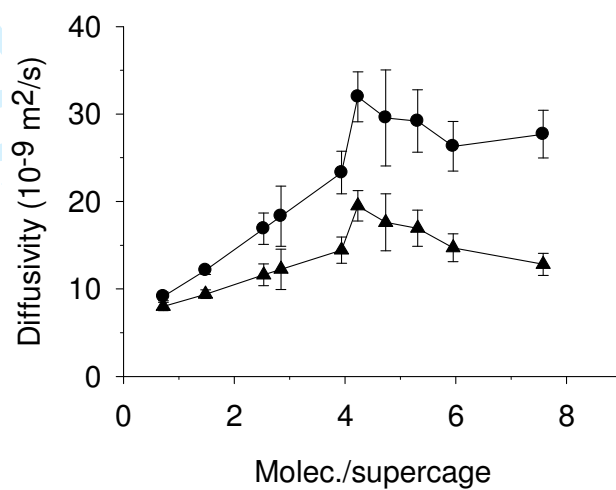


Fig. 15

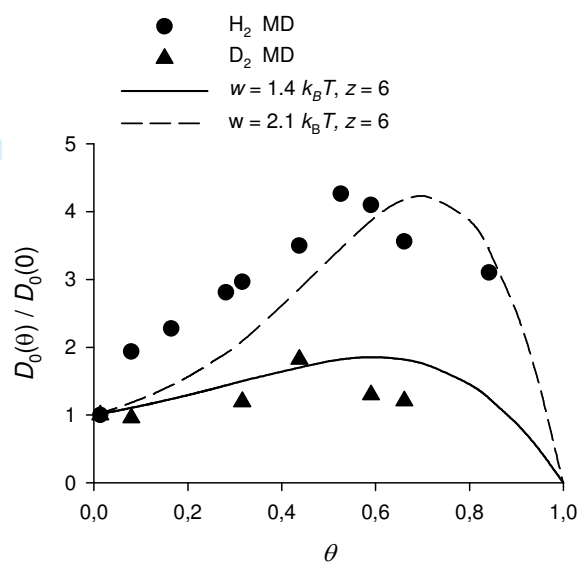


Fig. 16

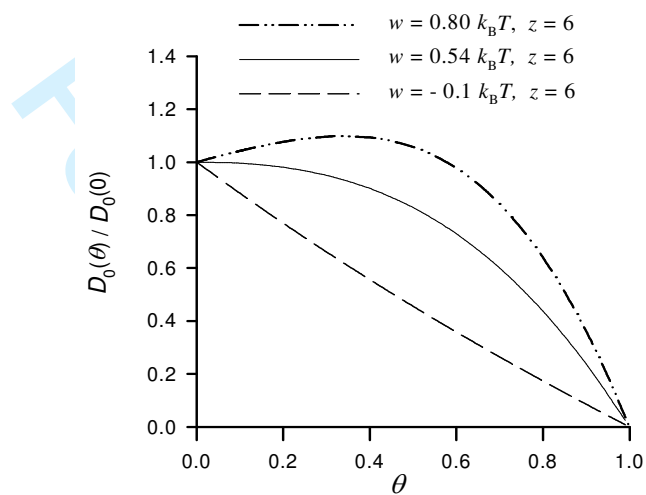


Fig. 17